HHS Public Access

Author manuscript

Nat Med. Author manuscript; available in PMC 2014 December 01.

Published in final edited form as:

Nat Med. 2014 June ; 20(6): 616–623. doi:10.1038/nm.3545.

Modeling the mitochondrial cardiomyopathy of Barth syndrome with iPSC and heart-on-chip technologies

Gang Wang[1,*], **Megan L. McCain**[2,*], **Luhan Yang**[2,3], **Aibin He**[1], **Francesco Silvio Pasqualini**[2], **Ashutosh Agarwal**[2], **Hongyan Yuan**[2], **Dawei Jiang**[1], **Donghui Zhang**[1], **Lior Zangi**[1], **Judith Geva**[1], **Amy E. Roberts**[1,4], **Qing Ma**[1], **Jian Ding**[1], **Jinghai Chen**[1], **Da-zhi Wang**[1], **Kai Li**[1], **Jiwu Wang**[5], **Ronald J. A. Wanders**[6], **Wim Kulik**[6], **Frédéric M. Vaz**[6], **Michael A. Laflamme**[7], **Charles E. Murry**[7,8], **Kenneth R. Chien**[9], **Richard I. Kelley**[10], **George M. Church**[2,3], **Kevin Kit Parker**[2,11,¥], and **William T. Pu**[1,11,¥]

[1]Department of Cardiology, Boston Children's Hospital, Boston, MA, 02115, USA [2]Wyss Institute for Biologically Inspired Engineering, School of Engineering and Applied Sciences, Harvard University, Cambridge, MA, 02138, USA [3]Department of Genetics, Harvard Medical School, Boston, MA, 02115, USA [4]Boston Children's Hospital Department of Medicine, Division of Genetics, Boston Children's Hospital, Boston, MA, 02115, USA [5]Allele Biotechnology & Pharmaceuticals, Inc., San Diego, CA, 92121, USA [6]Department of Clinical Chemistry and Pediatrics, Laboratory Genetic Metabolic Disease, Academic Medical Center, Amsterdam, 1105 AZ, The Netherlands [7]Department of Pathology, Center for Cardiovascular Biology and Institute for Stem Cell and Regenerative Medicine, University of Washington, Seattle, WA, 98109, USA [8]Departments of Bioengineering and Medicine/Cardiology, University of Washington, Seattle, WA, 98109, USA [9]Department of Cell and Molecular Biology and Medicine, Karolinska Institutet, 17177, Stockholm, Sweden [10]Division of Metabolism, Kennedy Krieger Institute, Baltimore, MD, 21205, USA [11]Harvard Stem Cell Institute, Harvard University, Cambridge, MA, 02138, USA

Abstract

¥Correspondence to: W.T.P. 300 Longwood Ave, Boston, MA 02115, USA. wpu@enders.tch.harvard.edu. Phone: 617-919-2091. Fax: 617-730-0140. K.K.P. 29 Oxford Street, Pierce Hall Cambridge, MA 02130, USA. kkparker@seas.harvard.edu. Phone: 617-495-2850. Fax: 617-496-1793.

*contributed equally

Author Contributions

GW designed and performed experiments and analyzed data. MLM designed and performed experiments on MTFs and sarcomere organization and analyzed data. Her contribution is equal to GW. LY and GMC provided expert assistance and reagents for genome editing. FSP designed the sarcomere organization analysis method. HY developed the MTF analysis method. AA assisted with MTF substrate fabrication and experiments. DJ provided advice on mitochondrial assays. DZ imaged iPSC-CMs to assess their mitochondrial organization and potential. LZ and KRC provided expert assistance with modRNA, and JD and DW helped constructed modRNAs. KL contributed to genome editing. RJAW, WK, and FMV analyzed phospholipids. MAL and CEM provided expert assistance in iPSC differentiation to cardiomyocytes. AH developed shTAZ viruses and provided technical assistance. RIK provided expert input and ^{31}P-NMR data. KKP and WTP supervised the study. WTP wrote the manuscript, and it was revised by KKP and GW.

Competing Financial Interests

Jiwu Wang is an employee of Allele Biotechnology & Pharmaceuticals, Inc.

Studying monogenic mitochondrial cardiomyopathies may yield insights into mitochondrial roles in cardiac development and disease. Here, we combine patient-derived and genetically engineered iPSCs with tissue engineering to elucidate the pathophysiology underlying the cardiomyopathy of Barth syndrome (BTHS), a mitochondrial disorder caused by mutation of the gene Tafazzin (TAZ). Using BTHS iPSC-derived cardiomyocytes (iPSC-CMs), we defined metabolic, structural, and functional abnormalities associated with TAZ mutation. BTHS iPSC-CMs assembled sparse and irregular sarcomeres, and engineered BTHS "heart on chip" tissues contracted weakly. Gene replacement and genome editing demonstrated that TAZ mutation is necessary and sufficient for these phenotypes. Sarcomere assembly and myocardial contraction abnormalities occurred in the context of normal whole cell ATP levels. Excess levels of reactive oxygen species mechanistically linked TAZ mutation to impaired cardiomyocyte function. Our study provides new insights into the pathogenesis of Barth syndrome, suggests new treatment strategies, and advances iPSC-based in vitro modeling of cardiomyopathy.

Barth syndrome (BTHS) is an X-linked cardiac and skeletal mitochondrial myopathy caused by mutation of the gene Tafazzin (*TAZ*)[1], an acyltransferase responsible for normal acylation of cardiolipin, the major phospholipid of the mitochondrial inner membrane[2] (Supplementary Fig. 1). Cardiolipin abnormalities are also seen in ischemic heart disease and aging and have been implicated in the cardiac dysfunction in these conditions[3]. The mechanisms that lead from abnormal cardiolipin biogenesis to cardiomyopathy are not well understood. Here, we combined patient-derived iPSCs, genome-edited iPSCs, modified RNA (modRNA)[4], and "heart on a chip"[5] technologies to replicate the pathophysiology of Barth syndrome (BTHS) cardiomyopathy in tissue constructs. Using these approaches, we identified mitochondrial functional abnormalities caused by TAZ mutation and cardiolipin deficiency. We show that TAZ mutation is necessary and sufficient to disrupt sarcomere assembly and contractile stress generation, and that these phenotypes are not due to global ATP depletion. Furthermore, we show that the BTHS cardiomyopathic phenotype is readily reversed by reintroduction of wild-type TAZ, or by suppression of excessive reactive oxygen species (ROS) produced by BTHS mitochondria. These results provide new insights into the links between mitochondrial function, sarcomere assembly, and muscle contractile activity and suggest new therapeutic strategies for BTHS.

An iPSC-CM model of Barth syndrome

To investigate BTHS pathogenesis in a controlled *in vitro* setting, we generated iPSCs from two unrelated individuals with Barth Syndrome. Two lines, BTH-H and BTH-C, reprogrammed using retroviral[6] or modified RNA approaches[7,8], respectively, had confirmed TAZ frameshift (c.517delG) and missense (c.328T>C) mutations, respectively. These iPSC lines had normal karyotype and met pluripotency criteria (Supplementary Fig. 2; all cell lines in this study are summarized in Supplementary Table 1). As controls, we used three normal iPSC lines, generated by retroviral (WT1 and WT2) or modified RNA (WT3) reprogramming (Supplementary Table 1). The experiments presented below were reproduced in multiple experiments and multiple cell lines with consistent results; due to space restrictions we provide representative data in the accompanying figures and

supplementary data and refer the reader to Supplementary Table 2 for an overview of the data collected.

We differentiated the iPSCs into iPSC-CMs using an established protocol[9] (Supplementary Fig. 3a–c), followed by magnetic cell sorting for the cardiomyocyte surface marker VCAM1[10,11] to yield preparations containing ~80% cardiomyocytes (Supplementary Fig. 3d–f). On replating, the enriched myocytes formed sheets of cardiomyocytes (Supplementary Fig. 3g) that beat spontaneously (Supplementary Movie 1).

BTHS is characterized by depletion of mature cardiolipin and accumulation of an immature form, monolysocardiolipin (Supplementary Fig. 1).[12,13] Phospholipid profiles of BTHS iPSC-CMs, measured by mass spectrometry, confirmed that BTHS iPSC-CMs replicated abnormal cardiolipin processing (Fig. 1a). The monolysocardiolipin to cardiolipin ratio in BTHS iPSC-CMs exceeded 0.3, the clinically used diagnostic threshold for BTHS[13] (Fig. 1a, b). Thus, BTHS iPSC-CMs exhibited impaired cardiolipin biogenesis that matched what is observed clinically in BTHS patients.

We assessed mitochondrial form and function in BTHS iPSC-CMs. By FACS analysis, BTHS iPSC-CMs had similar mitochondrial number compared control iPSC-CMs, and the size of BTHS iPSC-CM mitochondria was less than controls (Supplementary Fig. 4a,b). This corresponded to greater mitochondrial fragmentation of BTHS iPSC-CM mitochondria compared to the more highly networked mitochondria of controls (Fig. 4c). To assess BTHS mitochondrial function, we cultured iPSC-CMs in galactose-based media, which has limited ability to support ATP production via glycolysis.[14] Under these conditions, BTHS iPSC-CM ATP levels were significantly lower than controls (Fig. 1c). Consistent with cellular energy deprivation, AMP-dependent kinase (AMPK) was markedly activated in BTHS iPSC-CMs (Supplementary Fig. 5a). Next, we used an extracellular flux analyzer to probe mitochondrial function (approach and terms summarized in Supplementary Fig. 5b,c). BTHS iPSC-CMs unexpectedly exhibited elevated basal oxygen consumption rate, which was due to both increased F1F0 ATP synthase oxygen consumption and increased “H^+ leak” (Fig. 1d, e and Supplementary Fig. 5d). In the context of reduced basal ATP levels, these data pointed to inefficient F1F0 ATP synthase activity, which we confirmed by selective complex immunocapture followed by measurement of its quantity and activity (Supplementary Fig. 5e). Collectively, the data demonstrate that TAZ deficiency and consequent cardiolipin abnormalities reduce peak electron transport chain function and decrease ATP generating efficiency by lowering F1F0 ATP synthase specific activity.

We also measured maximal electron transport chain activity (“Respiratory Capacity”) and found that it was severely impaired in BTHS iPSC-CMs (Fig. 1d, e). The metabolic abnormalities of BTHS iPSC-CMs were not evident in BTHS primary fibroblasts or iPSCs (Supplementary Fig. 5f, g), consistent with the muscle-selective phenotype of BTHS patients.

Cardiomyocytes are capable of producing ATP through both glycolysis and oxidative phosphorylation. We hypothesized that glucose, an energy source that supports both glycolysis and oxidative phosphorylation, would normalize ATP levels. Indeed glucose

induced glycolysis and triggered a metabolic shift away from oxidative phosphorylation in both BTHS and control iPSC-CMs (Supplementary Fig. 5h,i). This metabolic shift normalized BTHS iPSC-CM ATP levels and basal oxygen consumption rate (Fig. 1f and Supplementary Fig. 5j). However, glucose culture did not correct the markedly depressed respiratory capacity of BTHS iPSC-CMs (Supplementary Fig. 5j). These observations indicate that glucose restores basal ATP levels through increased glycolysis, but does not correct underlying mitochondrial defects in the electron transport chain.

TAZ mutation causes BTHS iPSC-CM phenotypes

Because BTHS patient-derived and control iPSCs had numerous genetic differences other than TAZ mutation, we took three independent approaches to further establish the causative role of TAZ mutation in abnormal cardiolipin biogenesis and mitochondria function. First, we used adenoviral delivery of TAZ-specific short hairpin RNAs (shRNAs) to deplete TAZ in neonatal rat ventricular cardiomyocytes (NRVMs) by over 80% by 72 hours post-infection (Supplementary Fig. 6a). By this time point, cardiolipin profiles in TAZ knockdown NRVMs were already highly abnormal (Supplementary Fig. 6b), indicating rapid turnover of TAZ and mature cardiolipin. As in the BTHS iPSC-CMs, TAZ deficiency in NRVMs grown in galactose reduced ATP levels, activated AMPK (Supplementary Fig. 6c, d), and caused comparable abnormalities in mitochondrial function (Supplementary Fig. 6e). Electron microscopy did not reveal alterations in mitochondrial morphology or number in this short term TAZ depletion experiment (Supplementary Fig. 6f), suggesting that mitochondrial functional abnormalities are not contingent upon mitochondrial structural abnormalities observed in BTHS patients.

Second, we used a novel method to efficiently re-introduce TAZ into BTHS iPSC-CMs. Cardiomyocytes, including iPSC-CMs, are refractory to standard transfection methods. We synthesized TAZ mRNA, substituting 5-methylcytidine for cytidine, and pseudouridine for uridine[4,7,15]. This modified RNA ("modRNA") has minimal toxicity[4,7,15] and efficiently transfects cardiomyocytes (Supplementary Fig. 7). TAZ modRNA likewise transfected iPSC-CMs, and TAZ protein localized to mitochondria (Fig. 2a). TAZ modRNA restored cardiolipin biogenesis and normalized basal mitochondrial function in BTHS iPSC-CMs, although maximal respiratory capacity was rescued incompletely (Fig. 2b–e). These results indicate that TAZ mutation is necessary for the BTHS mitochondrial phenotype, and that this phenotype is rapidly reversed upon TAZ restoration.

Third, we used Cas9-mediated scarless genome editing[16] to mutate TAZ in the control human line PGP1-iPSC, yielding three iPSC lines that are isogenic except for the sequence of TAZ exon 6 (Supplementary Table 1 and Fig. 3a–c; see Methods and Supplementary Fig. 8 for details on construction and validation of these iPSC lines). PGP1-TAZ$^{c.517delG}$ contains the TAZ frameshift mutation from the BTH-H line (1 nt deletion), while PGP1-TAZ$^{c.517ins}$ contains a distinct frameshift mutation at the same site (14 nt insertion; Fig. 3a–c). PGP1-TAZ^{WT} is a control line handled in parallel to PGP1- TAZ$^{c.517delG}$ and PGP1-TAZ$^{c.517ins}$, but without a TAZ mutation. iPSC-CMs derived from these isogenic TAZ mutant lines fully recapitulated the cardiolipin, mitochondrial, and ATP deficits that we observed in patient-derived iPSCs and in the neonatal rat TAZ knockdown model (Fig. 3d–

g; Supplementary Table 2). Together, these data indicate that TAZ mutation alone is sufficient to cause these phenotypes in a wild-type genetic background.

Abnormal sarcomerogenesis in BTHS iPSC-CMs

Mitochondria regulate cardiomyocyte maturation[17], a hallmark of which is assembly of organized arrays of sarcomeres. We noticed that BTH-H iPSC-CMs grown on unpatterned gelatin substrate assembled sarcomeres irregularly compared to controls. To precisely compare sarcomere architecture, we engineered iPSC-CM shape by seeding the cells on micropatterned fibronectin rectangles designed to mimic the dimensions of human adult cardiomyocytes[18], with length:width ratios of approximately 7:1 (95 μm × 13 μm). To quantify the global regularity of sarcomere arrangement, we developed an unbiased metric to score images of patterned iPSC-CMs immunostained for the sarcomere protein α-actinin. This metric, which we named sarcomere organization, is based on the regularity of sarcomere spacing, as determined from 2-D Fourier spectra of the sarcomere immunostains (Supplementary Fig. 9a–c and Methods). While sarcomeres in control iPSC-CMs extended serially along the entire length of the cell, sarcomeres in patient-derived BTH-H iPSC-CMs were intermittent and sparse (Fig. 4a). Treatment with TAZ modRNA appeared to restore sarcomere regularity (Fig. 4a). These differences were reflected in the sarcomere organization metric, which was lower in BTH-H iPSC-CMs compared to control and was increased by TAZ modRNA treatment (Fig. 4a). Although glucose culture normalized ATP levels to a comparable degree compared to TAZ modRNA, glucose culture did not rescue sarcomere formation (Fig. 4a). These defects in sarcomere assembly were recapitulated in genome edited PGP1-TAZ$^{TAZc.517delG}$ and PGP1-TAZ$^{c.517ins}$ iPSC-CMs compared to isogenic PGP1-TAZ^{WT} controls (Fig. 4b), confirming the causative role of the BTH-H exon 6 frameshift TAZ mutation. These data suggest that sarcomerogenesis is sensitive to mitochondrial function independent of whole cell ATP levels.

Interestingly, BTH-C iPSC-CMs exhibited sarcomere organization that was not significantly different from controls (Fig. 4c). This phenotypic heterogeneity may be due to the specific BTH-C missense mutation, or it may be due other variables between cell lines. Further use of genome-edited cell lines will be necessary to better understand genotype-phenotype relationships in this disease.

Myocardial constructs model the BTHS myopathic phenotype and its genetic rescue

Because BTHS patients often develop cardiomyopathy, we asked if we could replicate the contractile pathophysiology of Barth Syndrome in an in vitro model of engineered myocardium and demonstrate the efficacy of TAZ modRNA treatment on the disease. Towards this goal, we used our “heart on a chip” assay[5,19] to quantitatively measure contractility of engineered myocardial tissue assembled from BTHS or control iPSC-CMs. MACS-selected iPSC-CMs were seeded onto thin elastomers micropatterned with fibronectin lines and supported by glass coverslips[20,21]. Over a five day culture period, the iPSC-CMs self-organized into laminar, anisotropic myocardium. Staining for sarcomeric α-actinin in control iPSC-CM tissues revealed both aligned sarcomeres and fibrous structures

indicative of the relatively immature phenotype of iPSC-CMs (Fig. 5a), similar to previous observations in immature primary rat cardiac myocytes.[22] Engineered BTHS iPSC-CM tissues continued to exhibit impaired sarcomere assembly compared to controls (Supplementary Fig. 10a). Pre-cut muscular thin film (MTF) tissue constructs were then peeled from the glass substrate, allowing them to contract and curl away from the plane of the coverslip (Fig. 5a; Supplementary Movie 2). Movies of contracting MTFs were used to calculate radii of curvature, from which we calculated the diastolic and peak systolic stresses using a modification of Stoney's equation[5,20,23]. Twitch stress was calculated as the difference between diastolic and peak systolic stress (Fig. 5a). During electrical field stimulation, control iPSC-CM MTFs contracted rhythmically at frequencies ranging from 1–5 Hz (Fig. 5b; Supplementary Fig. 10b; Supplementary Movie 2). Patient-derived, BTH-H iPSC-CM tissues were significantly weaker over the same stimulation frequency range, indicating that BTHS engineered myocardial tissue recapitulates the BTHS myopathic phenotype.

Next we asked if the engineered myocardial tissue constructs effectively model disease correction. Treatment of BTH-H iPSC-CMs (Fig. 5b, Supplementary Fig. 10, and Supplementary Movie 2) with TAZ modRNA for five days restored contractile function to levels comparable to controls, further confirming that this myopathic phenotype was reversible and due to TAZ mutation.

We assessed the contribution of whole cell ATP to BTHS contractile dysfunction by culturing engineered iPSC-CM MTF constructs in glucose, which increased BTHS cellular ATP levels to a level comparable to TAZ modRNA. In contrast to TAZ modRNA rescue, glucose culture alone did not restore BTH-H iPSC-CM force generation at any tested stimulation frequency (Fig. 5b, Supplementary Fig. 10b,c, and Supplementary Movie 3). Although local pools of mitochondrially produced ATP might theoretically be required for iPSC-CM force generation, such a mechanism is unlikely because inhibition of mitochondrial ATP production with oligomycin in control iPSC-CMs did not alter their contractile strength (Supplementary Fig. 11), consistent with their immature and highly glycolytic properties. Together, these data show that BTH-H iPSC-CMs have a severe defect in contractility that occurred independent of ATP depletion. This result is consistent with anectodal data from BTHS patients that show preserved cardiac high energy phosphate levels in the setting of impaired heart function (e.g., Supplementary Fig. 12), suggesting that contractile dysfunction in patients can occur despite normal myocardial energy stores.

The findings from patient-derived, BTH-H iPSC-CMs were reproduced in the isogenic, genome-edited cells. Contractile function of the mock-manipulated PGP1-TAZ^{WT} iPSC-CM myocardial constructs was equivalent to the parental PGP1 cell line, while TAZ disruption in both PGP1- TAZ$^{c.517delG}$ and PGP1- TAZ$^{c.517ins}$ caused severe loss of contractile stress generation (Fig. 5c; Supplementary Fig. 10c; Supplementary Movie 4). Reintroduction of TAZ by modRNA restored contractility to mutant tissues. Thus, in both patient-derived cells and cells with an isogenic background, TAZ deficiency induces contractile dysfunction.

BTH-C myocardial tissue constructs also showed poor contractile function, reflected in their markedly reduced beating activity (Supplementary Movie 2) and severely depressed twitch

stress (Fig. 5d). Systolic stress generation was also reduced significantly in BTH-C myocardial tissue constructs compared to controls (Fig. 5d). However, their peak systolic (and diastolic) stresses were substantially higher than their BTH-H counterparts (Fig. 5d vs 5b), perhaps reflecting the difference in sarcomere assembly that we observed between these TAZ genotypes (Fig. 4a vs. 4c).

Together, these results indicate that TAZ mutation is sufficient to cause a myopathic phenotype in myocardial tissue constructs, and that this phenotype is readily reversible upon TAZ replacement.

Assessment of potential therapies using BTHS iPSC-CMs

We used BTHS iPSC-CMs to measure the effect of three proposed interventions for Barth syndrome: bromoenol lactone, an inhibitor of mitochondrial phospholipase A_2, which catabolizes mature cardiolipin[24]; linoleic acid (LA), an essential unsaturated fatty acid precursor of mature cardiolipin[25]; and arginine plus cysteine, amino acids which are frequently deficient in BTHS patients[26]. LA and bromoenol lactone partially corrected the monolysocardiolipin to cardiolipin ratio, while arginine plus cysteine had no effect (Fig. 6a). Treatment of galactose-cultured BTHS iPSC-CMs with LA or arginine plus cysteine increased ATP to levels comparable to control or to TAZ modRNA rescue, while bromoenol lactone had no significant effect (Fig. 6b). LA, but not arginine plus cysteine, also normalized basal and F1F0 ATP synthase oxygen consumption rate of BTHS iPSC-CMs but had little effect on maximal mitochondrial respiratory capacity (Fig. 6c; Supplementary Fig. 13). Thus, of the three tested compounds, LA was most effective at correcting the metabolic phenotype of BTHS iPSC-CMs.

Because LA had a positive effect in each of these metabolic assays, we asked if LA supplementation would mitigate the sarcomere organization and contractile defects of BTHS-iPSC-CMs. LA improved sarcomere organization of BTH-H iPSC-CMs (Fig. 6d). No statistically significant improvement was noted in BTH-C iPSC-CMs, whose sarcomeric organization was not significantly different from controls. In both BTH-H and BTH-C myocardial tissue constructs, LA dramatically increased twitch stress to nearly normal levels (Fig. 6e). This was reflected in the obvious effect of LA on rhythmic beating of the BTHS myocardial MTF constructs (Supplementary Movie 5). Thus, LA rescued the contractile deficits of BTHS iPSC-CMs.

In addition to potentially enhancing alternative CL synthesis pathways, LA might also influence BTHS iPSC-CM phenotype by scavenging reactive oxygen species (ROS). Extensive literature implicates high levels of ROS in ischemic and hypertensive heart failure, in part through effects on sarcomere assemby and function.[27] Uncoupling of the electron tranport chain and elevated mitochondrial membrane potential, both observed in BTHS iPSC-CMs (Fig. 1 and Supplementary Fig. 14a–d), promote mitochondrial ROS production. Indeed, we found that mitochondrial ROS production was markedly increased in BTHS iPSC-CMs, as assessed by measurement of 4-hydroxynonenal (4-HNE), a product of lipid peroxidation, or by Mitosox, a mitochondrially targeted probe with ROS-enhanced fluorescence (Supplementary Fig. 14e). 4-HNE levels were suppressed to near baseline by

LA (Fig. 6f). To distinguish antioxidant from CL-precursor mechanisms of LA action, we tested the mitochondrially targeted and structurally unrelated antioxidant mitoTEMPO. Like LA, mitoTEMPO suppressed excessive ROS in BTHS iPSC-CMs (Fig. 6g).

Having confirmed that mitoTEMPO effectively suppresses excessive mitochondrial ROS in BTHS iPSC-CMs, we next determined if mitoTEMPO treatment improved sarcomere organization and force generation of these disease cardiomyocytes. Indeed, mitoTEMPO treatment normalized sarcomere organization and contractility of BTHS iPSC-CMs (Fig. 6h–i; Supplementary Movie 6).

These data indicate that iPSC-CMs and heart-on-chip technology enable effective in vitro testing of candidate therapeutic agents. Furthermore, these data link impaired sarcomerogenesis and weak force generation in BTHS iPSC-CMs to excessive ROS production.

Discussion

Patient-derived iPSCs have significant potential to enhance our understanding of human disease and enable therapeutic screening on a personalized basis. However, several barriers still hinder adoption of iPSC disease models academically, clinically, and commercially. One obstacle to wider use of iPSC disease models has been the genetic and epigenetic variation between cell lines, which introduces confounding variables that can be difficult to control. We show that Cas9-mediated genome editing is an excellent strategy to isolate a mutation of interest and show that it is sufficent to cause a disease phenotype. Gene replacement using modified RNA technology is another highly portable approach that demonstrates the acute requirement of a gene mutation for a disease phenotype within a given cell line.

Another major impediment to the use of iPSCs to study human disease pathogenesis has been the lack of in vitro models that reproduce disease pathophysiology. With respect to cardiomyopathies, modeling the contractile function of iPSC-CMs at the level of myocardial tissue has been challenging, and prior iPSC-based models of cardiomyopathy have focused on measurements of single cell contractile function[28,29]. Here, we assembled anisotropic, laminar myocardial tissue constructs from iPSC-CMs and used these to document impaired contractile stress generation in BTHS. Furthermore, we use this approach to model phenotypic rescue at the tissue level by gene replacement and small molecule treatments.

Our metabolic and functional analysis of human Barth syndrome cardiomyocytes elucidated mitochondrial functional impairment caused by mature cardiolipin depletion. Our data show that the contracile deficit of BTHS iPSC-CMs is not a result of global cellular energy depletion. Rather, we show that TAZ deficiency in BTHS impairs sarcomere assembly and contractile stress generation. It is likely that sarcomere assembly is only one of several factors that lead to reduced twitch stress in BTHS iPSC-CMs, since the extent of sarcomere disarray did not necessarily correlate with impairment of twitch stress across our assays.

We found that TAZ deficiency in BTHS caused markedly increased ROS production, and suppression of ROS normalized the metabolic, sarcomerogenesis, and contractile

phenotypes of BTHS iPSC-CMs. These data indicate that excessive ROS production contributes to sarcomere disarray and reduced contractile stress generation in BTHS iPSC-CMs. ROS has been implicated in cardiomyocyte differentiation, sarcomerogenesis, and contractility.[17,27] Our data indicate that ROS scavenging may be beneficial for BTHS patients and suggest that this strategy should be further validated using in vivo models. Our findings may be relevant to more common diseases such as ischemia and aging, since mature cardiolipin depletion and elevated ROS production also occur in these conditions[3].

Online Methods

Cell culture

Low passage skin fibroblasts were obtained from skin biopsies from two unrelated BTHS patients with informed consent under protocols approved by the Boston Children's Hospital Institutional Review Board. WT1 control cells were derived from BJ cells (Stemgent), while WT2 and WT3 were described previously[7,8,30]. The BTH-H iPSC line was established by retroviral delivery of four reprogramming factors (OCT4, SOX2, KLF4 and OCT4)[6]. The BTH-C iPSC line was established by modRNA reprogramming as described[7]. Several iPSC clones with ES cell morphology and with positive vital staining for TRA-1–81 or TRA-1–60 staining[31], were further characterized to yield the final two lines studied. Karyotyping was performed by Cell Line Genetics, Inc. Teratomas were formed by injection of 10^6 iPSCs intramuscularly into the flanks of adult SCID mice under protocols approved by the Boston Children's Hospital Institutional Animal Care and Use Committee. Teratomas were examined by H&E and immunofluorescent staining.

Cardiomyocyte differentiation was induced as previously reported[9], with minor modifications. Cells were detached by 3–5 min incubation with Versene (Invitrogen) and seeded onto Matrigel-coated plates at a density of 10,000 cells/cm^2 in murine embryonic fibroblast conditioned medium (MEF-CM) plus 4 ng/mL bFGF for 2–3 days before induction. Cells were covered with matrigel (1:60 dilution) on the day before induction. To induce cardiac differentiation, we replaced MEF-CM with RPMI+B27 medium (RPMI-1640, 2 mM L-glutamine, ×1 B27 supplement without insulin) supplemented with 100 ng/mL of Activin A (R&D Systems) for 24 hours, followed by 10 ng/mL human bone morphogenetic protein 4 (R&D) and 10 ng/mL human basic fibroblast growth factor for 4 days without culture medium changes. The culture medium was subsequently replaced with RPMI+B27 supplemented with 100 ng/mL of DKK1 (R&D) for 2 days. At day 7, the culture medium was changed to RPMI+B27 without supplementary cytokines; culture medium was refreshed every 1–2 days. Leibovitz L-15 medium was substituted for RPMI for galactose containing culture media.

For iPSC-CM enrichment, differentiation cultures were dissociated with Accumax (Innovative Cell Technologies). Dissociated cells were stained with anti-VCAM1 antibody (refer to Supplementary Table 1 for antibody information) conjugated with allophycocyanin (APC) and magnetically sorted using anti-APC microbeads (Miltenyi Biotec). For validation of MACS, sorted cells were fixed and stained with TNNT2-Alexa-488. Data were analyzed with FlowJo (Treestar) software.

NRVMs were isolated from neonatal rat heart ventricles by collagenase digestion using the Neomyts isolation kit (Cellutron). Procedures involving animals were performed under protocols approved by the Institutional Animal Care and Use Committee.

For MitoTEMPO treatment, iPSC-CMs were purified by VCAM1 MACS and reseeded on muscle thin films at 1 million cells per well of a six well plate (see below). The cells were treated with MitoTEMPO at a final concentration of 5 μM for 5 days.

Cas9 Genome Editing

Details of our modified Cas9 genome editing strategy will be published separately. In brief, we constructed a piggyBac transposon that expresses the reverse tet activator and a human codon optimized Cas9 under the control of a tet response element. Transient transfection of PGP1-iPSCs (Coriell) with piggyBac and this engineered transposon yielded PGP1iPSC-hCas9. We subsequently designed guide RNA and donor oligonucleotides (Fig. 3a–c; Supplementary Fig. 8; and Suppl. Table 4) to introduce the BTHH TAZ mutation into exon 6. After transient dox administration and transfection with gRNA and donor oligonucleotides, we screened individual clones by Sanger sequencing. We selected an unmodified clone, a clone containing the BTHH mutation (homologous recombination), and a clone containing a novel insertion due to non-homologous end joining. Transient piggyBac transfection subsequently led to removal of the Cas9-containing transposon.

TAZ sequencing

TAZ sequencing was performed using previously described primers[32], listed in Supplementary Table 4. Mutations are referenced to Refseq NM_000116.3.

Cardiac ^{31}P-NMR

Cardiac ^{31}P-NMR was performed as described[33]with informed consent under a protocol approved by the Institutional Review Board of the Children's Hospital of Philadelphia. High energy phosphate stores were estimated from the phosphocreatine peak area, normalized to the peak area from the β-phosphate of ATP[33].

Mitochondrial Function Assays

For mitochondrial function assays, 60,000 sorted cells were seeded in 0.1% gelatin-coated seahorse assay wells in alpha MEM (Invitrogen) with 10% FBS. They were then changed to L-15 media supplemented with 1× B27 supplement without insulin for 5–7 days. Oygen consumption rate (OCR) was measured using a Seahorses Biosciences XF24 extracellular flux analyzer and normalized to total protein, determined using the BCA protein assay (Thermo Scientific). OCR was expressed as pmol/min/10 μg protein. For ATP assays, cells were grown in indicated media and supplements for 5 days. ATP assay reagent (Promega) was added directly to wells and light output was measured with a plate luminometer. Readout was normalized to total protein.

Mitochondrial Isolation and FACS Analysis

Mitochondrial isolation and FACS analysis were performed to measure mitochondrial size, number, membrane potential, and production of reactive oxygen species. Mitochondrial

isolation and FACS were performed based on described protocols.28studying its in vivo relevance to angiogenesis.his mechanistic hypothesis is being specifically tested by Dr. Zhang. He is al[34] In brief, iPSC-CMs were digested to single cells by Versene and mitochondria were isolated using the Mitochondria Isolation Kit (Thermo Scientific). 20 millions iPSC-CMs were pelleted by centrifugation at 850g for 2 minutes. The pellet was resuspended in 800 μl of mitochondria isolation reagent A with protease inhibitor. The suspension was vortexed at medium speed for 5 seconds and then incubated on ice for exactly 2 minutes. Then 10 μl mitochondria isolation reagent B was added and vortexed at maximum speed for 5 seconds. After 5 minutes incubation on ice with vortexing at maximum speed every minute, 800 μl mitochondria isolation reagent C with protease inhibitor was added. The tube was centrifuged at 700g for 10 minutes at 4°C. The supernatant was transferred to a new microfuge tube and centrifuged at 3000g for 15 minutes. The supernatant was discarded and 500 μl mitochondria isolation reagent C was added to the pellet. The sample was then centrifuged at 12000g for 5 minutes. The mitochondria pellet was resuspended in 200 μl FACS buffer (Stemcell Technologies Inc). Either MitoSox (5 μM) or TMRM (100 nM) and Mitotracker Green (50 nM) were incubated with mitochondria for at room temperature for 30 minutes. The sample was then analyzed by flow cytometry. Data were analyzed by using Flowjo software.

shRNA adenovirus

Control and TAZ shRNA viruses were constructed as described previously[35] using sequences provided in Supplementary Table 4.

Imaging and Gene expression analysis

Immunostaining for marker expression was performed using antibodies listed in Supplementary Table 3. Samples were fixed in 4% paraformaldehyde and permeabilized with 0.05% Triton X-100. Imaging was performed on an Olympus FV1000 or Zeiss LSM 5 LIVE confocal microscope. qRTPCR was performed from total RNA using primers listed in Supplementary Table 4. Sybr green chemistry was used for real time PCR detection on an ABI 7500 instrument.

Mitochondria were labeled using BacMam 2.0 mitochondria-RFP (Invitrogen), in which baculovirus delivers RFP tagged with the mitochondrial localization sequence of E1 alpha pyruvate dehydrogenase.

Electron microscopy was performed on a Tecnai G Spirit BioTWIN instrument. At least 10 randomly selected fields containing cardiomyocytes were imaged per sample.

Modified RNA synthesis and delivery

The iPSC reprogramming cDNA templates were obtained from Addgene[7]. The TAZ modRNA cDNA template was expressed from pcDNA3.3-TOPO-T7–5’UTR-cMyc-3’UTR, which contains the T7 promoter and optimized 5’ and 3’ untranslated regions (Addgene plasmid 26818)[7]. The vector was modified to place unique AscI and NheI restriction sites between the 5’ and 3’ untranslated regions. Full length human TAZ cDNA corresponding to Refseq NM_000116 with a 5’ FLAG tag was cloned into modified vector.

To synthesize the modRNA, the UTRs and ORF were PCR amplified using a polyA-tailed primer. 1.6 μg of purified PCR productwas transcribed in a 40 μl reaction system using the MEGAscript T7 kit (Ambion, Austin, TX) and a custom ribonucleoside cocktail from Allele Biotechnology (No. ABP-PP-NTPMIX), containing pseudouridine-5′-triphosphate, Methylcytidine-5′-triphosphate, GTP, ATP, and ARCA (Cap Analog). Reactions were incubated 6 hr at 37°C. After DNase treatment RNA was purified with Ambion MEGAclear spin columns, then treated with Antarctic Phosphatase (New England Biolabs) for 30 min at 37°C. Treated RNA was repurified and adjusted to 100 ng/mL working concentration with Tris-EDTA (pH 7.0).

Modified mRNA transfection were performed with RNAiMAX (Invitrogen). Transfection media was supplemented with 200 ng/ml B18R interferon inhibitor (eBioscience). After 4 hours, the transfection medium was replaced with fresh culture medium containing 200 ng/ml B18R.

Microcontact Printing

Standard soft lithography techniques were used to fabricate polydimethylsiloxane (PDMS) stamps for microcontact printing (Sylgard 184, Dow Corning Midland, MI), as previously described[36,37]. Briefly, a silicon wafer was spun coat with SU-8 3005 (MicroChem Corp., Newton, MA) and selectively exposed to UV light using a photomask. After being developed, the wafer was used as a template for PDMS stamps. For the single cell studies, we used stamps with 95 μm ×13 μm rectangles. For the muscular thin film studies, we used stamps with 15 μm wide lines separated by 2 μm.

To measure sarcomere organization in single cell studies, glass coverslips (diameter 18 mm) were spun coat with PDMS and cured. PDMS stamps were coated with 50 μg/mL fibronectin (BD Biosciences, San Jose, CA) for one hour, dried, and inverted onto the coverslips after treatment in a UVO cleaner (Jelight Company Inc., Irvine, CA). Stamps were removed and the coverslips were incubated in 1% F127 Pluronic Acid (BASF, Mount Olive, NJ) for at least five minutes before rinsing with PBS and storage at 4°C. MACS-purified iPSC-CMs were plated on microfabricated fibronectin islands for five days and transfected daily with the indicated modRNA.

Quantitation of Sarcomere Organization

For quantitation of sarcomere organization of iPSC-CM plated on fibronectin islands, images of single myocytes stained for sarcomeric α-actinin were analyzed using custom-designed software in ImageJ (NIH, Bethesda, MD) and MATLAB (Mathworks, Natick, MA). Images were pre-processed to highlight the filamentous structure of the cytoskeleton using a tubeness operator[38], which replaces each pixel in the image with the largest non-positive eigenvalue of the image Hessian matrix. To calculate the ability of single cells to spread across the microcontact printed islands, the convex hulls[39] of sarcomeric α-actinin and fibronectin binarized immunostains were obtained and utilized to calculate cell projected surface area.

The regularity of spacing between the cytoskeletal elements that stained positive for sarcomeric α-actinin (Supplementary Fig. 9 Ai and Bi) was assessed by first considering the

magnitude of the oscillatory portion of the 2D Fourier transform of pre-processed and binarized immunostains (Supplementary Fig. 9 Aii and Bii):

$$F(u,v)=\Im\{f(x,y)\}\int_{R^2}\int f(x,y)e^{-j2\pi(ux+vy)}dxdy \quad (1)$$

To fully automate the analysis and remove any user-bias[40], 512 radial profiles of the 2D Fourier transform were summed to obtain a 1D representation – $\Gamma(\omega_n)$ – of the 2D spectrum (blue-dots in Supplementary Fig. 9 Aiii and Biii) that was further normalized so that the total area under the curve would be 1. A least square minimization was performed to find the vector of parameters γ for which the function $\tilde{\Gamma}(\omega,\lambda)$ best fit the N experimental data points:

$$\tilde{\Gamma}(\omega,\gamma)=\tilde{\Gamma}_{ap}(\omega,\gamma_{ap})+\tilde{\Gamma}_{p}(\omega,\gamma_{p}) \quad (2)$$

$$\gamma=\min_{\gamma}[\sum_{n=1}^{N}\left(\Gamma(\omega_n)-\tilde{\Gamma}(\omega_n,\gamma)\right)^2] \quad (3)$$

The functional form of $\Gamma(\omega,\lambda)$ was composed by an aperiodic component, representing the effect of poorly developed cytoskeletal structures (black curve, Equation (4)) and a periodic component (red curves, Equation (5)) relating to periodically spaced Z-disks:

$$\tilde{\Gamma}_{ap}(\omega,\gamma_{ap})=a+be^{-c\omega};\gamma_{ap}=\{a,b,c\} \quad (4)$$

$$\tilde{\Gamma}_{p}(\omega,\gamma_{p})=\sum_{k=1}^{5}a_k e^{-\left(\frac{\omega-k\omega_0}{\delta_k}\right)^2};\gamma_{ap}=\{\omega_0,a_k,\delta_k\} \quad (5)$$

In agreement with Fourier analysis, the periodic component was approximated with a series of Gaussian peaks localized at integer multiples of the spatial frequency ($\omega_0 = 1/r_0$) associated with the sarcomere length ($r_0 \sim 2$ μm).

The area under the peaks of the periodic component was taken as a metric of structural organization and named sarcomere organization: that is, the organization increases as more sarcomeric α-actinin positive elements become localized in the Z-disks, at a distance ~r_0. We normalized all sarcomere organization values to the maximum value observed across all single cells before plotting.

Muscular Thin Film Fabrication and Experiments

Muscular thin film (MTF) chips were fabricated on 22 mm × 22 mm × 0.13–0.16 mm thick glass coverslips (Ted Pella Inc., Redding, CA).[19,20] Coverslips were covered with low adhesion Scotch tape (3M, St. Paul, MN) and two rectangles of dimensions 18 mm × 5.8 mm spaced 8.6 mm apart (center to center distance) were cut into the tape with a 10.6 micron wavelength CO_2 laser prototyping system (VersaLaser 2.0, 10W, Universal Laser systems, Scottsdale, AZ). Cut rectangles were peeled using a sharp tweezer and then 10%

(w/v) solution of poly(N-isopropylacrylamide), PIPAAm, (Polysciences, Inc., Warrington, PA) in 99% butanol was spun coat at 6000 rpm for 1 minute. This allowed the PIPAAm deposition within bare glass regions. The rest of the tape was then peeled off and PDMS mixed at 10:1 base to curing agent ratio was spun coat at 4000 rpm for 1 minute. PDMS-coated chips were placed in a 65°C for at least 8 hours to allow complete curing of the elastomer. Young's modulus in compression of the cured Sylgard 184 mixed in the ratio of 10:1 base to curing agent ratio was determined to be 1.52 ± 0.05 MPa (N = 18 samples, Mean ± Standard deviation) using an Instron 3342 mechanical apparatus (Instron, Norwick, MA). In the final step, two rows of cantilever outlines were cut into the elastomer within the PIPAAm rectangular regions such that the final cantilevers were 5 mm × 2 mm, or 3 mm × 2mm,spaced 2.5 mm apart (center to center distance).[19] For each batch of films, the thickness of the elastomer was measured using a profilometer (Dektak 6M, Veeco Instruments Inc., Plainview, NY) and found to be in the range of 11.4–13.4 μm.

MACS-purified iPSC-CMs were seeded on MTF constructs at a density of $10^5/cm^2$ and allowed to develop for five days, with daily transfection with modRNA as indicated. For contraction assays, MTF constructs were transferred to 37°C Tyorde's buffer solution (1.8 mM $CaCl_2$, 5 mM HEPES, 1 mM $MgCl_2$, 5.4 mM KCl, 135 mM NaCl, 0.33 mM NaH_2PO_4, and either 5 mM glucose or galactose depending on the experimental conditions, pH 7.4) and placed on the stage of a Zeiss Discovery V8 Stereo Microscope at room temperature. Tweezers were used to manually peel each thin film away from the glass coverslip as the PIPAAm layer dissolved due to the slight drop in temperature. When all films were peeled, the constructs were re-warmed to 37°C and paced with platinum field stimulation electrodes. Films were paced at 1, 2, 3, 4, and 5 Hz and their movement was recorded from above at 100 frames per second. Films paced at 2 Hz were used for statistical comparison because this frequency was closest to the spontaneous beat rate.

MTF stress quantitation

The longitudinal planar projections of contracting MTFs were automatically detected using custom ImageJ (NIH, Bethesda, MD) software and used to calculate the radius of curvature of each film using custom MATLAB (Mathworks, Natick, MA) software, as previously described.[5] The stress of the cell layer was determined from the radius of curvature using a modified form of Stoney's equation:

$$\sigma_{cell}=\frac{Et_s^2}{6\,(1-v^2)\,Rt_c\,(1+t_c/t_s)}. \quad (6)$$

where σ_{cell} is the stress of the cell layer, E, v and t_s are the Young's modulus, Poisson's ratio, and thickness of the PDMS film, respectively, R is MTF radius of curvature, and t_c is cell layer thickness. Equation (6) can be readily derived based on the theory of the cylindrical bending of thin plates[41] and the static equilibrium of the force and torque of plate bending[42]. Note that the plate modulus $E/(1 - v^2)$ instead of the biaxial modulus $E/(1 - v)$, appears in equation (6) because the anisotropic contraction of the cell layer bends the PDMS film into a cylindrical shape instead of a bowl-like shape. The factor $(1 + t_c/t_s)^{-1}$ is a correction to the standard Stoney's equation[42] when the thickness of the cell layer

approaches that of the PDMS layer. We previously used a more comprehensive model[23] to calculate not only the stress in the film but also the shortening of the muscle layer. For the MTFs used in this paper, the stresses calculated by these two methods are almost identical, so we chose to adopt the simpler analytical form of the modified Stoney's equation.

Stress values failed the Shapiro-Wilkinson test for normality and were thus statistically compared using Kruskal-Wallis One-Way ANOVA on Ranks and Dunn's method for pairwise comparisons. Tests with a p-value less than 0.05 were considered statistically significant.

Supplementary Material

Refer to Web version on PubMed Central for supplementary material.

Acknowledgements

This work was funded by support from the Barth Syndrome Foundation, the Boston Children's Hospital Translational Investigator Service, the NHLBI Progenitor Cell Biology Consortium (NIH U01 HL100401 and U01 HL100408), NIH RC1 HL099618, NIH UH2 TR000522, and charitable donations from Edward Marram, Karen Carpenter, and Gail Federici Smith.

References

1. Bione S, et al. A novel X-linked gene, G4.5. is responsible for Barth syndrome. Nat Genet. 1996; 12:385–389. [PubMed: 8630491]
2. Houtkooper RH, et al. The enigmatic role of tafazzin in cardiolipin metabolism. Biochim Biophys Acta. 2009; 1788:2003–2014. [PubMed: 19619503]
3. Chicco AJ, Sparagna GC. Role of cardiolipin alterations in mitochondrial dysfunction and disease. Am J Physiol Cell Physiol. 2007; 292:C33–C44. [PubMed: 16899548]
4. Kariko K, Buckstein M, Ni H, Weissman D. Suppression of RNA recognition by Toll-like receptors: the impact of nucleoside modification and the evolutionary origin of RNA. Immunity. 2005; 23:165–175. [PubMed: 16111635]
5. Grosberg A, Alford PW, McCain ML, Parker KK. Ensembles of engineered cardiac tissues for physiological and pharmacological study: heart on a chip. Lab Chip. 2011; 11:4165–4173. [PubMed: 22072288]
6. Takahashi K, et al. Induction of pluripotent stem cells from adult human fibroblasts by defined factors. Cell. 2007; 131:861–872. [PubMed: 18035408]
7. Warren L, et al. Highly efficient reprogramming to pluripotency and directed differentiation of human cells with synthetic modified mRNA. Cell Stem Cell. 2010; 7:618–630. [PubMed: 20888316]
8. Warren L, Ni Y, Wang J, Guo X. Feeder-free derivation of human induced pluripotent stem cells with messenger RNA. Sci Rep. 2012; 2:657. [PubMed: 22984641]
9. Shiba Y, et al. Human ES-cell-derived cardiomyocytes electrically couple and suppress arrhythmias in injured hearts. Nature. 2012; 489:322–325. [PubMed: 22864415]
10. Uosaki H, et al. Efficient and scalable purification of cardiomyocytes from human embryonic and induced pluripotent stem cells by VCAM1 surface expression. PLoS One. 2011; 6:e23657. [PubMed: 21876760]
11. Elliott DA, et al. NKX2-5(eGFP/w) hESCs for isolation of human cardiac progenitors and cardiomyocytes. Nat Methods. 2011; 8:1037–1040. [PubMed: 22020065]
12. Schlame M, et al. Phospholipid abnormalities in children with Barth syndrome. Journal of the American College of Cardiology. 2003; 42:1994. [PubMed: 14662265]

13. Kulik W, et al. Bloodspot assay using HPLC-tandem mass spectrometry for detection of Barth syndrome. Clin Chem. 2008; 54:371–378. [PubMed: 18070816]
14. Rana P, Anson B, Engle S, Will Y. Characterization of human-induced pluripotent stem cell-derived cardiomyocytes: bioenergetics and utilization in safety screening. Toxicol Sci. 2012; 130:117–131. [PubMed: 22843568]
15. Kariko K, et al. Incorporation of pseudouridine into mRNA yields superior nonimmunogenic vector with increased translational capacity and biological stability. Mol Ther. 2008; 16:1833–1840. [PubMed: 18797453]
16. Mali P, et al. RNA-Guided Human Genome Engineering via Cas9. Science. 2013
17. Hom JR, et al. The permeability transition pore controls cardiac mitochondrial maturation and myocyte differentiation. Dev Cell. 2011; 21:469–478. [PubMed: 21920313]
18. Gerdes AM, Capasso JM. Structural remodeling and mechanical dysfunction of cardiac myocytes in heart failure. J Mol Cell Cardiol. 1995; 27:849–856. [PubMed: 7602601]
19. Agarwal A, Goss JA, Cho A, McCain ML, Parker KK. Microfluidic heart on a chip for higher throughput pharmacological studies. Lab Chip. 2013; 13:3599–3608. [PubMed: 23807141]
20. Feinberg AW, et al. Muscular thin films for building actuators and powering devices. Science. 2007; 317:1366–1370. [PubMed: 17823347]
21. Domian IJ, et al. Generation of functional ventricular heart muscle from mouse ventricular progenitor cells. Science. 2009; 326:426–429. [PubMed: 19833966]
22. Parker KK, Tan J, Chen CS, Tung L. Myofibrillar architecture in engineered cardiac myocytes. Circ Res. 2008; 103:340–342. [PubMed: 18635822]
23. Alford PW, Feinberg AW, Sheehy SP, Parker KK. Biohybrid thin films for measuring contractility in engineered cardiovascular muscle. Biomaterials. 2010; 31:3613–3621. [PubMed: 20149449]
24. Malhotra A, et al. Role of calcium-independent phospholipase A2 in the pathogenesis of Barth syndrome. Proc Natl Acad Sci U S A. 2009; 106:2337–2341. [PubMed: 19164547]
25. Valianpour F, et al. Linoleic acid supplementation of Barth syndrome fibroblasts restores cardiolipin levels: implications for treatment. J Lipid Res. 2003; 44:560–566. [PubMed: 12562862]
26. Rigaud C, et al. Natural history of Barth syndrome: a national cohort study of 22 patients. Orphanet J Rare Dis. 2013; 8:70. [PubMed: 23656970]
27. Steinberg SF. Oxidative stress and sarcomeric proteins. Circ Res. 2013; 112:393–405. [PubMed: 23329794]
28. Sun N, et al. Patient-specific induced pluripotent stem cells as a model for familial dilated cardiomyopathy. Sci Transl Med. 2012; 4:130ra47.
29. Lan F, et al. Abnormal calcium handling properties underlie familial hypertrophic cardiomyopathy pathology in patient-specific induced pluripotent stem cells. Cell Stem Cell. 2013; 12:101–113. [PubMed: 23290139]

Online Methods References

30. Park IH, et al. Disease-specific induced pluripotent stem cells. Cell. 2008; 134:877–886. [PubMed: 18691744]
31. Chan EM, et al. Live cell imaging distinguishes bona fide human iPS cells from partially reprogrammed cells. Nat Biotechnol. 2009; 27:1033–1037. [PubMed: 19826408]
32. Ichida F, et al. Novel gene mutations in patients with left ventricular noncompaction or Barth syndrome. Circulation. 2001; 103:1256–1263. [PubMed: 11238270]
33. Whitman GJ, et al. Diagnosis and therapeutic evaluation of a pediatric case of cardiomyopathy using phosphorus-31 nuclear magnetic resonance spectroscopy. J Am Coll Cardiol. 1985; 5:745–749. [PubMed: 3156172]
34. Chen Y, Dorn GWn. PINK1-phosphorylated mitofusin 2 is a Parkin receptor for culling damaged mitochondria. Science. 2013; 340:471–475. [PubMed: 23620051]

35. He A, Kong SW, Ma Q, Pu WT. Co-occupancy by multiple cardiac transcription factors identifies transcriptional enhancers active in heart. Proc Natl Acad Sci U S A. 2011; 108:5632–5637. [PubMed: 21415370]

36. Bray MA, Sheehy SP, Parker KK. Sarcomere alignment is regulated by myocyte shape. Cell Motil Cytoskeleton. 2008; 65:641–651. [PubMed: 18561184]

37. Chen CS, Mrksich M, Huang S, Whitesides GM, Ingber DE. Geometric control of cell life and death. Science. 1997; 276:1425–1428. [PubMed: 9162012]

38. Sato Y, et al. Three-dimensional multi-scale line filter for segmentation and visualization of curvilinear structures in medical images. Med Image Anal. 1998; 2:143–168. [PubMed: 10646760]

39. Melkman AA. On-line construction of the convex hull of a simple polyline. Information Processing Ltters. 1987; 25:11–12.

40. Wei S, et al. T-tubule remodeling during transition from hypertrophy to heart failure. Circ Res. 2010; 107:520–531. [PubMed: 20576937]

41. Timoshenko, S.; Woinowsky-Krieger, S. Engineering societies monographs. Vol. 5. New York: McGraw-Hill; 1959.

42. Stoney GG. The Tension of Metallic Films Deposited by Electrolysis. Proceedings of the Royal Society A: Mathematical, Physical and Engineering Sciences. 1909; 82:172–175.

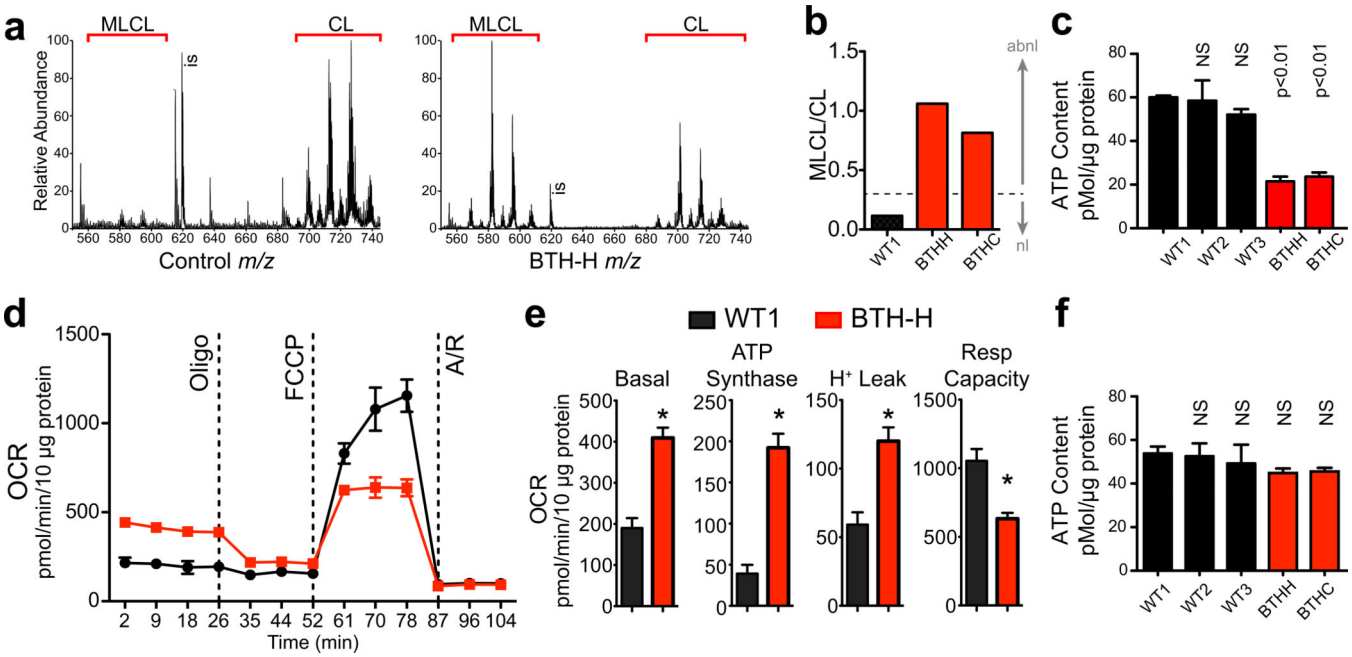

Fig. 1. Mitochondrial abnormalities in BTHS iCMs

a. Mass spectrum of control and BTH-H phospholipids showing mature cardiolipin (CL) and immature cardiolipin (monolysocardiolipin; MLCL) content of BTHS vs control iPSC-CMs.

b. Comparison of MLCL/CL ratio in BTH-H, BTH-C, and control iPSC-CMs. The dashed line indicates the clinical diagnostic threshold for BTHS.

c. ATP levels in BTHS and control iPSC-CMs cultured in galactose. n=3. NS, not significant.

d–e. Assessment of BTH-H and control iPSC-CM mitochondrial function in galactose culture. Function was measured using cellular oxygen consumption rate (OCR), normalized to total protein. Oligo, oligomycin. FCCP, carbonyl cyanide-4-(trifluoromethoxy)phenylhydrazone. A/R, antimycin plus rotenone. Measures of mitochondrial function (defined in Supplementary Fig. 5b,c) were quantitatively compared between control and BTH-H iCMs. n=3. *, P<0.05.

f. ATP levels in BTHS and control iPSC-CMs cultured in glucose. n=3.

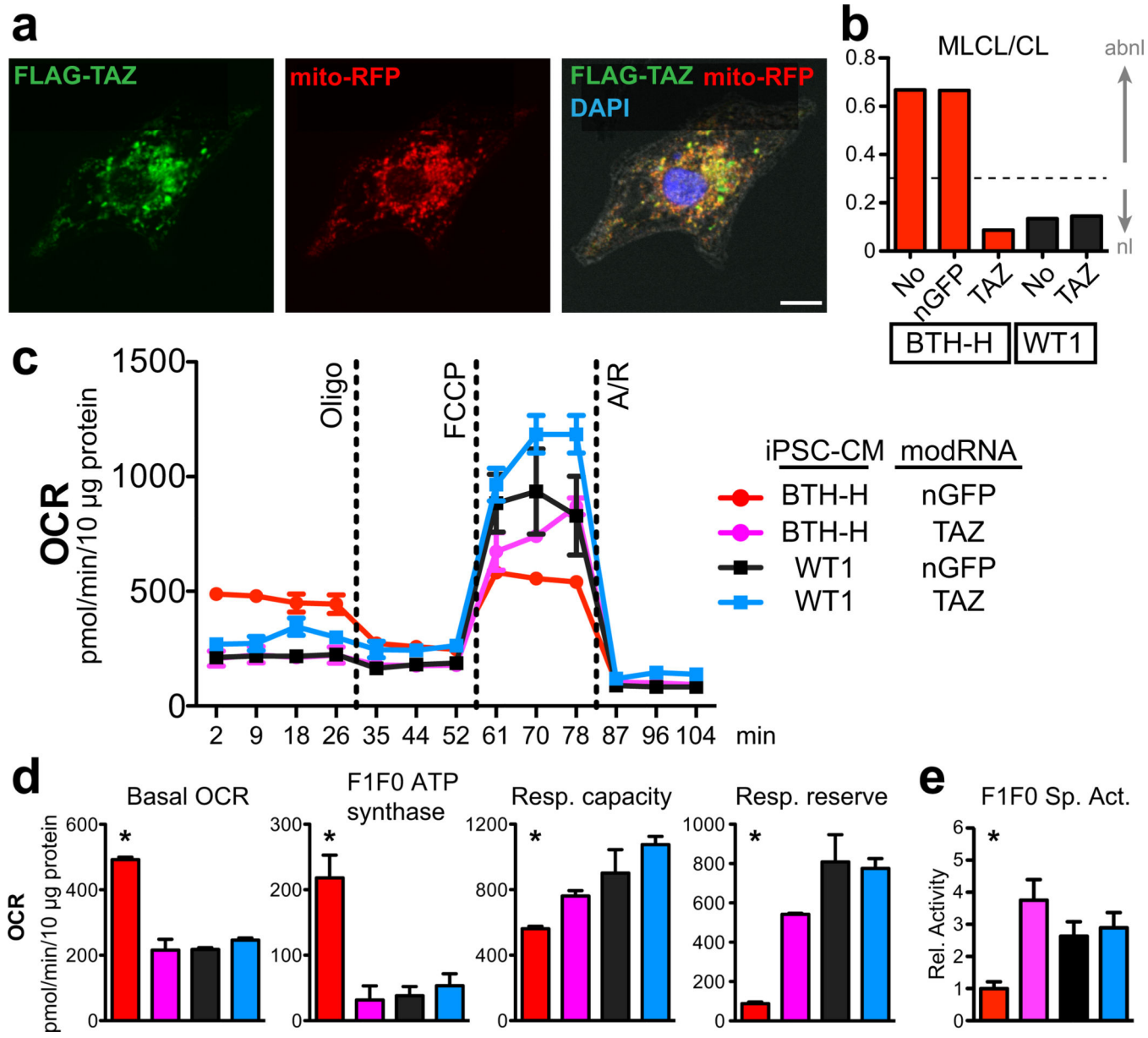

Fig. 2. TAZ deficiency is necessary to cause the iPSC-CM metabolic phenotype

a. Subcellular localization of FLAG-tagged TAZ, delivered to iPSC-CMs by modified RNA (modRNA) transfection. Localization to mitochondria was assessed by co-localization with virally delivered RFP targeted to mitochondria. FLAG co-localized with RFP. Bar = 10 µm.

b. TAZ modRNA restored cardiolipin biogenesis. BTH-H or control iPSC-CMs were transfected with the indicated modRNA and cardiolipin composition was measured by mass spectroscopy. MLCL/CL below 0.3 (dotted line) is considered normal.

c. Effect of TAZ modRNA on mitochondrial function in control and BTHS iPSC-CMs. Mitochondrial function was measured by extracellular flux analysis as detailed in Supplementary Fig. 5b,c.

d. Quantitation of mitochondrial functional parameters from c. n=3.

e. F1F0 ATP synthase specific activity, measured by selective complex immunocapture. n=6.

*, $P<0.05$ compared to each other group.

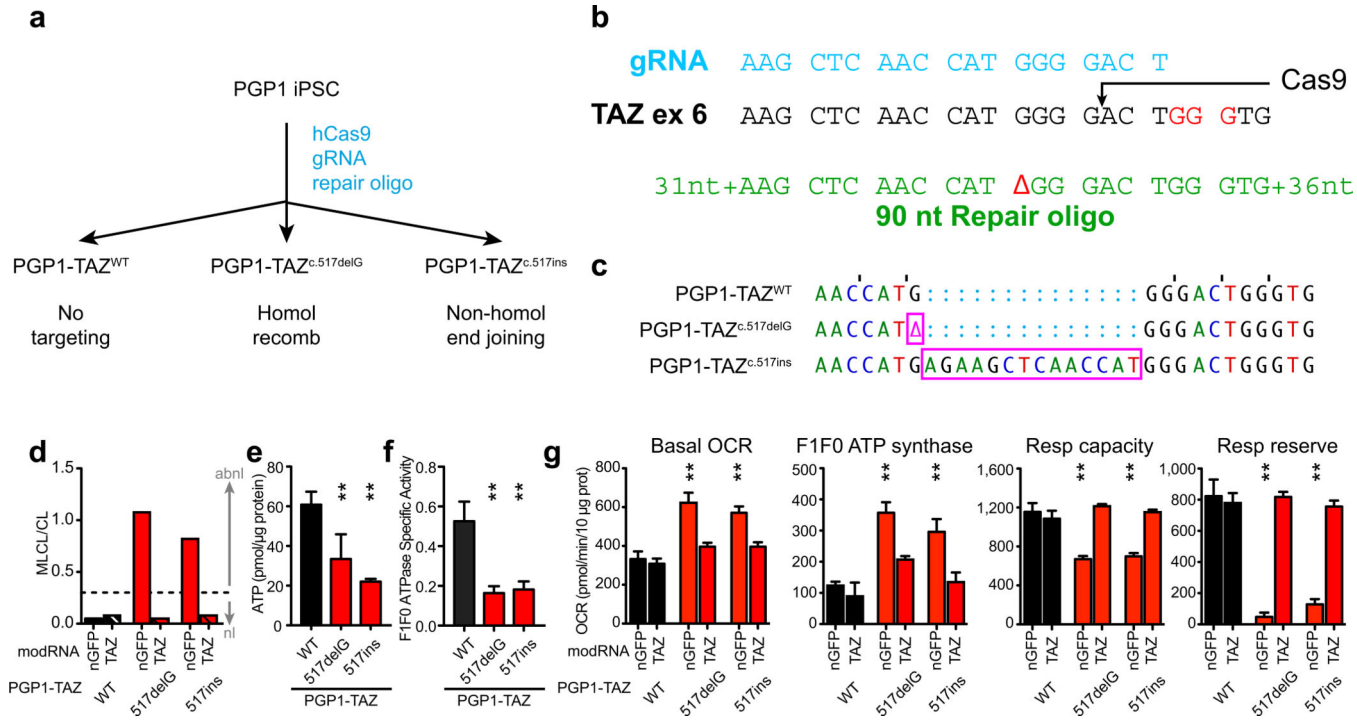

Fig. 3. Construction and characterization of TAZ mutant and isogenic control iPSCs by Cas9-mediated genome editing

a. Schematic of genome editing strategy.

b. Strategy for modification of TAZ exon 6 using Cas9, the indicated guide RNA (gRNA), and the indicated repair oligo.

c. Sequence of a region of TAZ exon 6 in selected genome-edited cell lines. Purple boxes indicate deletion (Δ) or insertion. PGP1-TAZ^{WT} was handled in parallel but was not modified and had wild-type TAZ sequence.

d. Cardiolipin maturation in TAZ and isogenic control iPSC-CMs, as determined by phospholipid mass spectroscopy.

e. Basal ATP level of TAZ mutant and isogenic control iPSC-CMs cultured in galactose media. **, p<0.01. n=3.

f. F1F0 ATPase specific activity, measured from selectively immunocaptured proteins, in TAZ mutant and isogenic control iPSC-CMs. **, p<0.01. n=3.

g. Abnormalities of mitochondrial function in TAZ mutant iPSC-CMs, as measured by extracellular flux mitochondrial function assay. iPSC-CMs were transfected with the indicated modified RNA for 5 days. **, p<0.01 by 1-way ANOVA with Dunnett's post-hoc test compared to PGP1-TAZ^{WT}+nGFP. n=3.

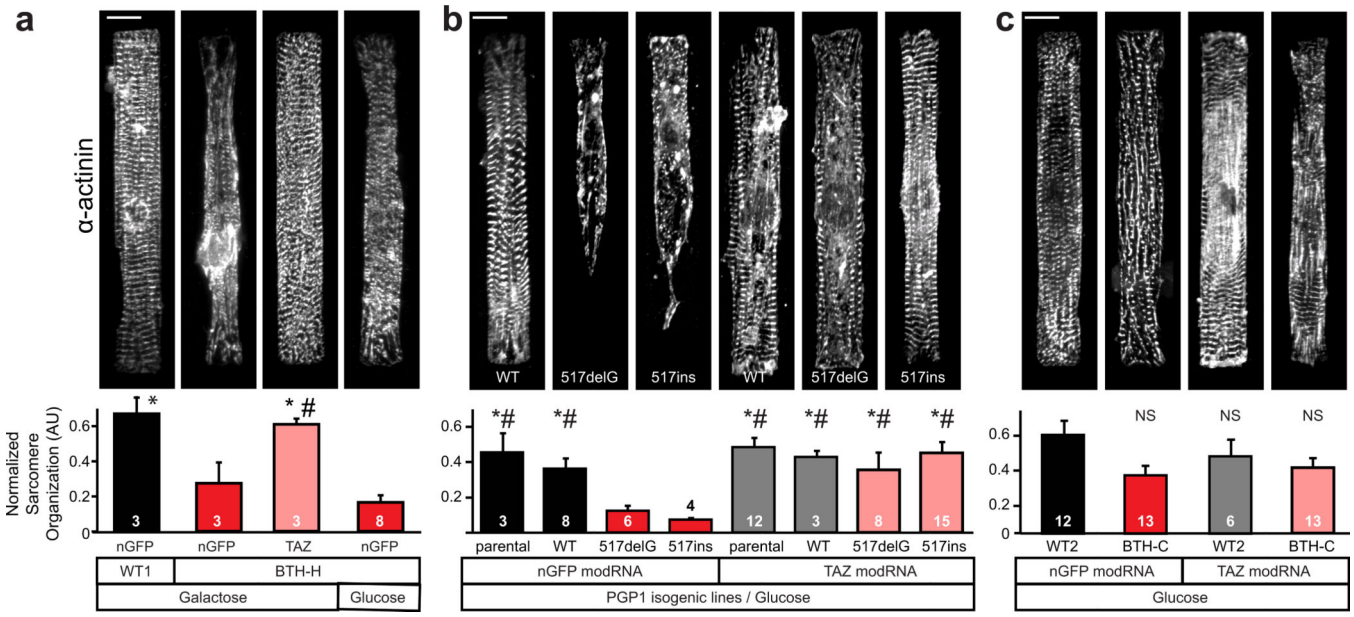

Figure 4. Impaired sarcomere organization in BTHH mutant iPSC-CMs

iPSC-CMs were seeded on micropatterned fibronectin rectangles with length:width ratios of 7:1 (95 μm × 13 μm), fixed, and stained for α-actinin. Sarcomere organization was quantitated by an unbiased 2D Fourier transform-based algorithm (see Supplemental Methods). Bar = 10 μm.

a. Sarcomere organization of patient-derived BTH-H and control iPSC-CMs. Sarcomere organization was tested in the indicated culture medium and after transfection with the indicated modified RNA. $P < 0.05$ vs: *, BTH-H + nGFP, gal; #, BTH-H + nGFP, glu.

b. Sarcomere organization of genome-edited, isogenic PGP1 iPSC-CMs containing the indicated TAZ variant. iPSC-CMs were transfected with the indicated modified RNA. $P < 0.05$ vs: *, PGP1-TAZ-517delG + nGFP; #, PGP1-TAZ-517ins.

c. Sarcomere organization of patient-derived BTH-C and control iPSC-CMs.

Statistical comparisons were made by ANOVA with Fisher LSD post-hoc test. NS, not significant. Sample number is displayed within each bar.

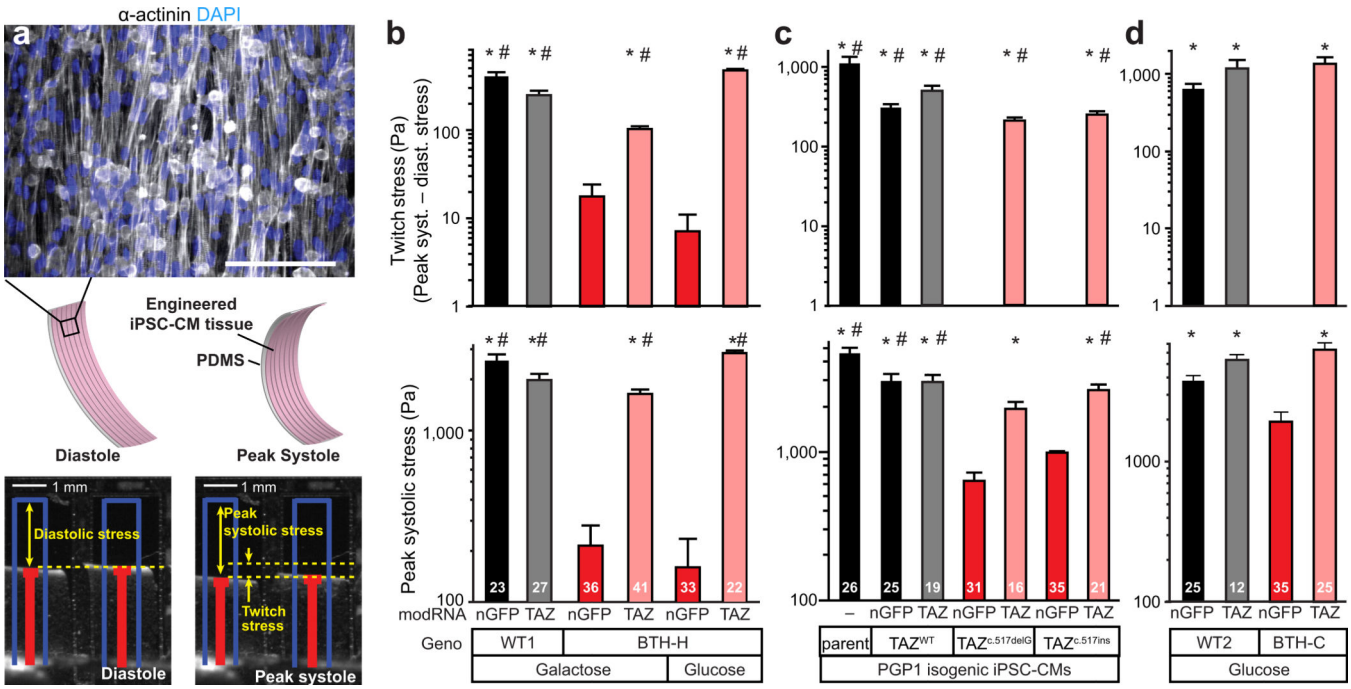

Figure 5. Depressed contractile stress generation by BTHS myocardial tissue constructs

a. iPSC-CMs seeded onto thin elastomers with patterned lines of fibronectin self-organized into anisotropic myocardial tissues referred to muscular thin films (MTFs). Cardiomyocyte stress generation reduces the radius of curvature of the construct as it contracts from diastole to peak systole. Red lines indicate automated MTF tracking projected onto the horizontal plane. Blue lines indicate lengths of MTFs prior to peeling from substrate. Bar, 100 μm.

b–d. Twitch stress and peak systolic stress generated by MTFs from patient-derived BTH-H and control iPSC-CMs (b), genome-edited TAZ frameshift and control iPSC-CMs (c), and patient-derived BTH-C and control iPSCs (d) at 2 Hz pacing. (b) $P<0.05$ vs: *, BTHH +nGFP, gal; #, BTH-H+nGFP+glu. (c) $P<0.05$ vs: *, PGP1-TAZ$^{c.517delG}$+nGFP; #, PGP1-TAZ$^{c.517ins}$+nGFP. (d) *, $P<0.05$ vs: BTH-C+nGFP.

Statistical comparisons were made by Kruskal-Wallis One Way ANOVA on ranks and Dunn's post-hoc test. Sample size is indicated by number inside each bar.

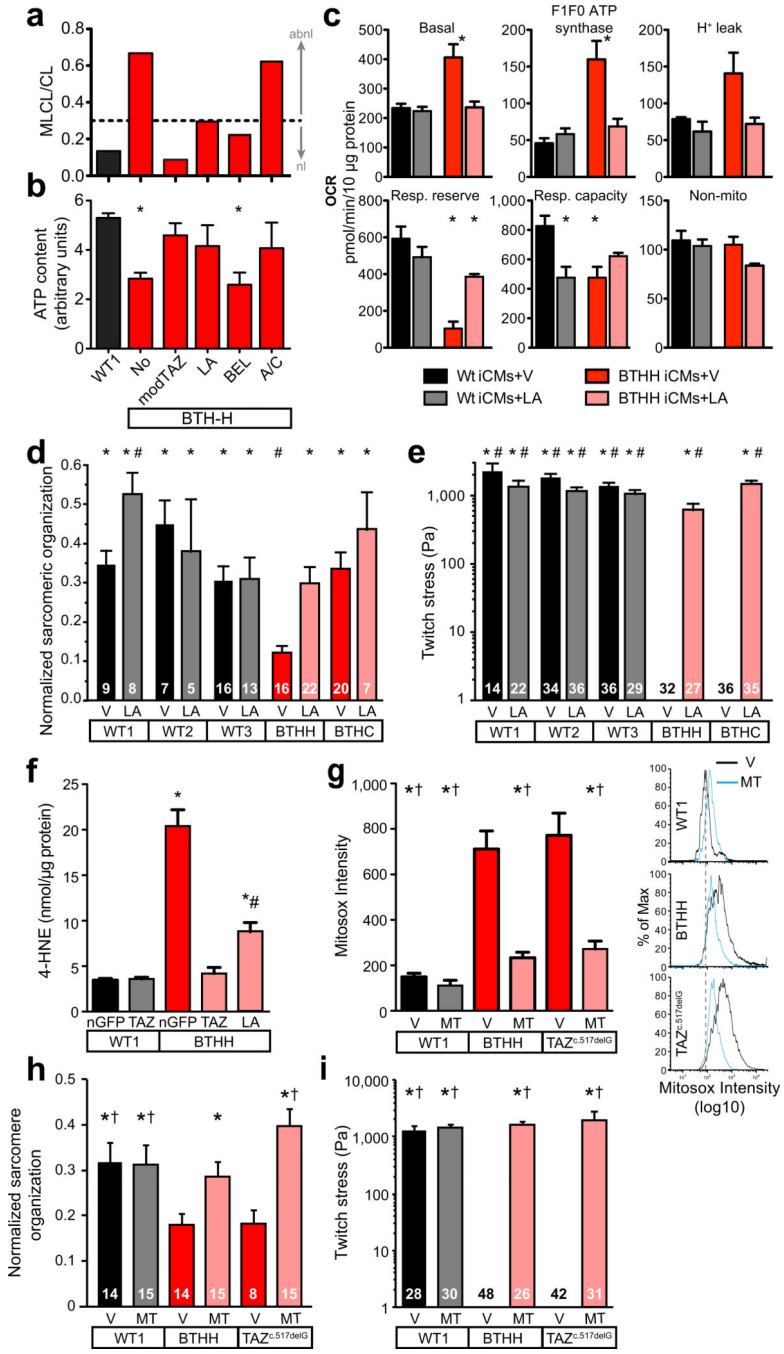

Fig. 6. Effect of small molecules on BTHS iCM ATP levels and mitochondrial function

a–c. BTHS iCMs were treated with linoleic acid (LA), bromoenol lactone (BEL), or arginine plus cysteine (A/C) for 5 days in galactose-containing media, and the effect on cardiolipin maturation (a), cellular ATP levels (b, n=3), and mitochondrial function (c, n=3) were measured. *, P<0.05 vs. control. V, vehicle.

d. Effect of LA treatment on sarcomeric organization compared to vehicle (V). LA increased BTHH sarcomeric organization but did not have a significant effect on BTHC sarcomeres. One-way ANOVA. P < 0.05 vs: *, BTHH + V; #, BTHC + V.

e. Effect of LA treatment on muscular thin film contractile stress generation. Twitch strength of BTHH and BTHC constructs were dramatically enhanced by LA treatment compared to vehicle (V). Kruskal-Wallis with Dunn's post-hoc test. Numbers inside bars indicate sample size. $P < 0.05$ vs: *, BTHH + V; #, BTHC + V

f. Lipid peroxidation in BTHS and control iPSC-CMs. Cells were cultured in glucose and treated with LA and the indicated modRNA for 5 days. The lipid peroxidation product 4-hydroxynonenal was measured by ELISA. One-way ANOVA. n=6. *, $P<0.05$ vs *, WT1 + nGFP; #, BTHH + nGFP.

g. Mitochondrial ROS in BTHS and control iPSC-CMs and its suppression by MitoTEMPO. Cells were treated with MitoTEMPO (MT) or vehicle (V). Mitochondrial ROS was assessed by FACS measurement of Mitosox fluorescence of isolated mitochondria. Representative histograms are shown to the right, with dotted line indicating the peak MitoSox signal intensity from WT1+V. One-way ANOVA. n=3. $P<0.05$ vs *, BTHH + V; †, PGP1-TAZ$^{c.517delG}$ + V.

h. Effect of MitoTEMPO on sarcomeric organization of iPSC-CMs plated on fibronectin rectangles. Numbers inside bars indicate cells analyzed. One-way ANOVA. $P<0.05$ vs *, BTHH + V; †, PGP1-TAZ$^{c.517delG}$ + V.

i. Effect of MitoTEMPO on force generation by iPSC-CM myocardial tissue constructs. Numbers inside bars indicate thin films analyzed. Kruskal-Wallis with Dunn's post-hoc test. $P<0.05$ vs *, BTHH + V; †, PGP1-TAZ$^{c.517delG}$ + V.